Investigation of the Residual in Column-Integrated Atmospheric Energy Balance Using Cloud Objects

SEIJI KATO, KUAN-MAN XU, TAKMENG WONG, AND NORMAN G. LOEB

NASA Langley Research Center, Hampton, Virginia

FRED G. ROSE

Science Systems and Applications Inc., Hampton, Virginia

KEVIN E. TRENBERTH

National Center for Atmospheric Research,[a] Boulder, Colorado

TYLER J. THORSEN

NASA Langley Research Center, and NASA Postdoctoral Program, Hampton, Virginia

(Manuscript received 5 November 2015, in final form 19 July 2016)

ABSTRACT

Observationally based atmospheric energy balance is analyzed using Clouds and the Earth's Radiant Energy System (CERES)-derived TOA and surface irradiance, Global Precipitation Climatology Project (GPCP)-derived precipitation, dry static and kinetic energy tendency and divergence estimated from ERA-Interim, and surface sensible heat flux from SeaFlux. The residual tends to be negative over the tropics and positive over midlatitudes. A negative residual implies that the precipitation rate is too small, divergence is too large, or radiative cooling is too large. The residual of atmospheric energy is spatially and temporally correlated with cloud objects to identify cloud types associated with the residual. Spatially, shallow cumulus, cirrostratus, and deep convective cloud-object occurrence are positively correlated with the absolute value of the residual. The temporal correlation coefficient between the number of deep convective cloud objects and individual energy components, net atmospheric irradiance, precipitation rate, and the sum of dry static and kinetic energy divergence and their tendency over the western Pacific are 0.84, 0.95, and 0.93, respectively. However, when all energy components are added, the atmospheric energy residual over the tropical Pacific is temporally correlated well with the number of shallow cumulus cloud objects over tropical Pacific. Because shallow cumulus alters not enough atmospheric energy compared to the residual, this suggests the following: 1) if retrieval errors associated with deep convective clouds are causing the column-integrated atmospheric energy residual, the errors vary among individual deep convective clouds, and 2) it is possible that the residual is associated with processes in which shallow cumulus clouds affect deep convective clouds and hence atmospheric energy budget over the tropical western Pacific.

1. Introduction

Horizontally and vertically nonuniform energy distribution received from the sun over the globe is the driver of atmospheric dynamics and the hydrological cycle. Solar radiation absorbed by the earth is converted into various different energy forms, and the earth emits infrared radiation that escapes back into space (Trenberth and Stepaniak 2004). All energy forms are related by the conservation of energy. Once radiative forcing alters the radiative component of the energy balance, it affects other

Denotes Open Access content.

Supplemental information related to this paper is available at the Journals Online website: http://dx.doi.org/10.1175/JCLI-D-15-0782.s1.

[a] The National Center for Atmospheric Research is sponsored by the National Science Foundation.

Corresponding author address: Seiji Kato, NASA Langley Research Center, Mail Stop 420, Hampton, VA 23681-2199.
E-mail: seiji.kato@nasa.gov

DOI: 10.1175/JCLI-D-15-0782.1

© 2016 American Meteorological Society

components. For example, several studies show that although the water vapor amount changes according to the Clausius–Clapeyron relationship when lower-tropospheric temperature is increased, the precipitation amount change is smaller because, for an annual and global mean, latent heat release by precipitation must be balanced by the surface sensible heat flux and net atmospheric irradiance (Held and Soden 2006; Stephens and Ellis 2008; Lambert and Webb 2008).

Although the conservation of energy is fundamental, studies with recent satellite observations indicate that a significant surface energy residual exists when observationally based surface irradiances, sensible and latent heat fluxes, and ocean heating rate are used (Kato et al. 2011; Stephens et al. 2012; Loeb et al. 2014). The sum of global annual mean net surface irradiance and sensible and latent heat fluxes significantly differs from the ocean warming rate inferred from ocean temperature measurements. As a result, in order to balance the surface energy budget Trenberth et al. (2009) chose to adjust the surface downward longwave irradiance, which increased the irradiance by about $12\,\mathrm{W\,m^{-2}}$ from the value estimated more recently from satellite observations. The uncertainty (1σ) in the global annual mean surface downward longwave irradiance estimated by Kato et al. (2012) in the Clouds and the Earth's Radiant Energy System (CERES) Energy Balanced and Filled (EBAF) surface product is $7\,\mathrm{W\,m^{-2}}$. Similarly, Stephens et al. (2012) chose to increase the surface latent heat flux by about $12\,\mathrm{W\,m^{-2}}$. This is equivalent to increasing the precipitation rate by about 16%. The uncertainty in the global mean precipitation derived by the Global Precipitation Climatology Project (GPCP) is less than 9% (Adler et al. 2012). Although the residual of the surface energy budget is too large for one component to eliminate it, L'Ecuyer et al. (2015) show that once all components are adjusted within their uncertainties, the global surface energy budget can be balanced. While the result of L'Ecuyer et al. (2015) is encouraging, the question remains why the observation-based energy budget does not balance. In addition, L'Ecuyer et al. (2015) also point out that the residual on a regional scale (e.g., the size of a continent) often exceeds the sum of uncertainties of all components.

Earlier studies focused on annual global mean values in evaluating the surface energy balance. In this study, we investigate where the residual occurs. While identifying regions with a large residual does not directly answer the question of why the current observationally derived surface energy budget does not balance, it might be possible to identify cloud systems or weather regimes, or both, that are associated with the large energy-budget residuals. This can help narrow down the processes or retrieval errors responsible for the residual. In the following sections, we start by discussing an atmospheric energy balance equation that is used to determine residual in section 2. Datasets used in this study are described in section 3. Atmospheric energy-budget residual and uncertainty estimates are presented in section 4. Cloud types associated with larger residuals over the tropics are identified in section 5.

2. Framework of atmospheric energy budget

We use the atmospheric energy budget instead of the surface energy budget to identify problematic regions in balancing the energy budget. This eliminates uncertainties in ocean heat transport but replaces them with uncertainties in horizontal energy transport in the atmosphere. Derivation of atmospheric energy balance equations is given by, for example, Vallis (2006) and Peixoto and Oort (1992) in z coordinates and by Boer (1982), Trenberth (1997), Trenberth and Stepaniak (2003a), and Trenberth and Smith (2009) in pressure coordinates. The vertically integrated atmospheric energy equations and assumptions made in deriving them are summarized in the appendix.

In this study, we use the vertically integrated atmospheric energy balance equation:

$$\frac{1}{g}\frac{\partial}{\partial t}\int_0^{p_s}(c_pT+\Phi_s+k)\,dp+\frac{1}{g}\nabla_p\cdot\int_0^{p_s}\mathbf{U}(c_pT+\Phi+k)\,dp = (R_T-R_s)+LP-F_{\mathrm{sh}}, \tag{1}$$

where g is acceleration due to gravity, c_p is the specific heat of air at constant pressure, Φ is the geopotential, k is kinetic energy, p is the pressure, $\mathbf{U}$ is the horizontal wind vector in pressure coordinates, R is the net (shortwave + longwave) irradiance, L is the latent heat of vaporization, P is the precipitation rate, and F_{sh} is the surface sensible heat flux. Subscripts T and s indicate top of atmosphere and surface, respectively. The irradiance and sensible heat flux are defined positive downward. The dry static energy is defined by $c_pT+\Phi$. An advantage of using Eq. (1) as opposed to Eq. (A14) is that three large terms to achieve the balance are precipitation, atmospheric net irradiance R_T-R_s, and dry static and kinetic energy divergence. In Eq. (1) energy terms that are associated with water are represented by precipitation multiplied by latent heat of vaporization. Another advantage is that the uncertainty in the precipitation estimate is probably better quantified (e.g., Adler et al. 2012) than the uncertainty in the surface latent heat flux. The dependence of the latent heat on water phase and temperature is ignored in Eq. (1) because L is constant in this study. The error introduced by

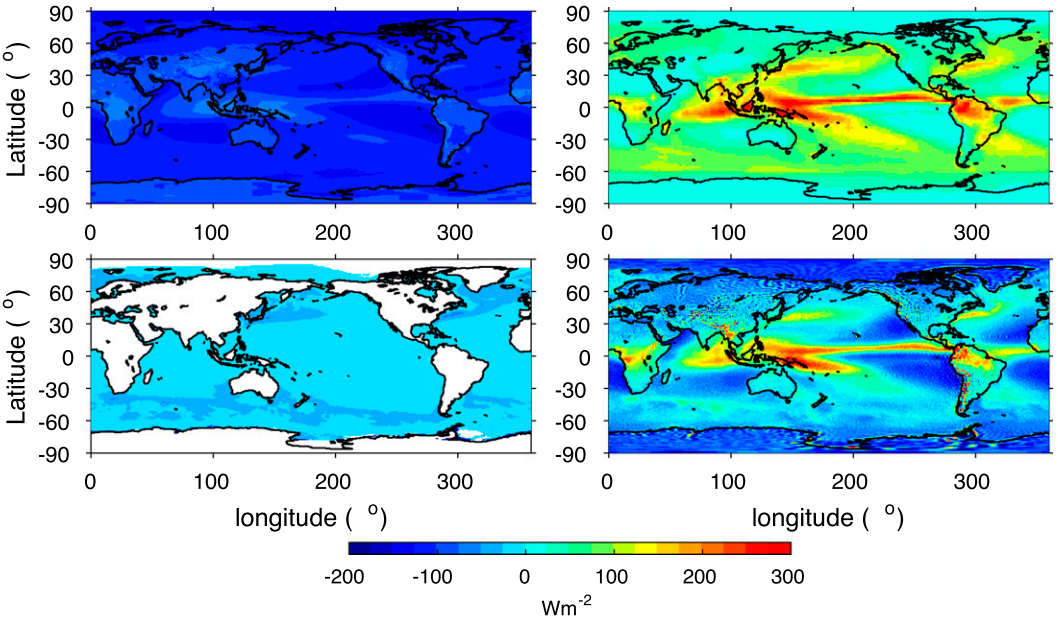

FIG. 1. (top left) Monthly mean atmospheric net irradiance (TOA net minus surface net, positive downward) derived from Ed2.8 of the EBAF data product, (top right) precipitation rate from GPCP V2.2 multiplied by latent heat of vaporization, (bottom left) sensible heat flux (positive downward) from SeaFlux, and (bottom right) dry static energy divergence derived from ERA-Interim. Monthly means are averaged from March 2000 through February 2010 except that sensible heat fluxes are averaged from January 2000 through December 2007.

ignoring water phase in L is small; the global mean error is approximately 0.5 W m^{-2} (Loeb et al. 2016), although the error can be approximately 10 W m^{-2} over polar regions. In addition, condensation that does not lead to precipitation is ignored in the water mass balance.

3. Datasets

We investigate regional atmospheric energy balance by Eq. (1) observationally in this study. We focus on the balance over ocean because the residual over land is small (section 4). The atmospheric net irradiance is computed with Ed2.8 of CERES EBAF-TOA (Loeb et al. 2009, 2012) and EBAF-surface (Kato et al. 2013). EBAF-TOA contains shortwave and longwave irradiances derived from radiance observations by CERES instruments on *Terra* and *Aqua*. The net TOA irradiance is constrained by ocean heating rate derived from Argo in situ ocean heat storage measurements (Loeb et al. 2009). Surface irradiances in EBAF-surface are consistent with TOA irradiances within a framework of one-dimensional (1D) radiative transfer theory (Kato et al. 2013). Precipitation rate is from GPCP version 2.2 (V2.2; Huffman et al. 1997; Adler et al. 2012). Precipitation rates are estimated combined from various observations, including microwave by SSM/I, infrared from geostationary and polar orbit satellites, Television and Infrared Observation Satellite (TIROS), Atmospheric Infrared Sounder (AIRS), and surface rain gauges (Adler et al. 2012). We use 28.94 W m^{-2} (mm day^{-1})$^{-1}$ to convert precipitation from millimeters per day to watts per meter squared. The surface sensible heat flux is from version 1 of SeaFlux (Clayson et al. 2016, manuscript submitted to *Int. J. Climatol.*). The SeaFlux product is only available from January 2000 through December 2007, but the rest of datasets cover the period from March 2000 through February 2010. The divergence and tendency terms are from ERA-Interim derived by Trenberth et al. (2011). Divergences are computed by vertically integrating over the atmospheric column using model levels and consequently computing the divergence (Trenberth 1997). All fluxes are averaged over a month in 5° × 5° grids to compute the atmospheric energy balance. Figure 1 shows four energy components used in Eq. (1). Because the surface sensible heat flux is generally small compared with other terms except over Kuroshio and Gulf Stream and the divergence of kinetic energy (not shown) as well as energy tendency are also small, the regional balance for a larger time scale (annual or larger) is essentially achieved by three terms—atmospheric net irradiance, precipitation, and divergence of dry static energy (Trenberth and Stepaniak 2003b). Note that the contribution of divergence goes to zero for the global mean,

resulting in the balance among atmospheric net irradiance, precipitation, and surface sensible heat flux.

4. Regional atmospheric energy-budget residual and uncertainty estimate

In principle, the annual mean surface net irradiance and latent and sensible heat fluxes nearly balances over land, as changes in storage are small. Over ocean, the sum of these components is equal to the ocean heating rate and energy transport by the ocean. When energy components are estimated from satellite observation individually, a residual occurs as a result of bias errors in the estimates. A study by L'Ecuyer et al. (2015) demonstrates that the residual of surface energy budget over land is much smaller than the residual of energy balance over ocean. To check how the atmospheric energy over ocean and land balances, we apply Eq. (1) over ocean and land separately and also separated by regions given by L'Ecuyer et al. (2015). In computing atmospheric energy balance over land, we use surface sensible heat fluxes averaged over regions given by L'Ecuyer et al. (2015), which are from Vinukollu et al. (2011).

Figure 2 shows the residual of atmospheric energy budget over land and ocean averaged over 10 years separated by regions. We compute energy budget residual ε using the following:

$$-\frac{1}{g}\frac{\partial}{\partial t}\int_0^{p_s}(c_pT+\Phi_s+k)\,dp - \frac{1}{g}\nabla_p\cdot\int_0^{p_s}\mathbf{U}(c_pT+\Phi+k)\,dp + (R_{\mathrm{TOA}}-R_{\mathrm{sfc}})+LP-F_{\mathrm{sh}}=\varepsilon. \quad (2)$$

While the energy budget residual in flux units over South America and Antarctica is larger than other land regions, when these fluxes are multiplied by the area, it is clear that larger residuals exist over ocean regions (Fig. 2). Once all regions are added, the energy residuals over land and ocean are 0.36 and −4.5 PW, respectively. Therefore, we focus on the residual of atmospheric energy budget over ocean for the rest of this study.

Figure 3 shows that ε computed with Eq. (2) over 5° × 5° averaged over 10 years is not uniform over oceans. The residual ε tends to be negative over tropics but positive over midlatitudes (Figs. 3 and 4). For the tropics, 12% of 5° × 5° grids have ε exceeding $-50\,\mathrm{W\,m^{-2}}$ (Fig. 4). Large absolute values of negative ε are present over the western and central tropical Pacific. Using a similar set of observations, Loeb et al. (2014) also found a larger residual of the atmospheric energy over the ascending branch of the Hadley circulation than descending branches of the Hadley circulation. When ε is averaged over the global ocean, it is $-12\,\mathrm{W\,m^{-2}}$ (Table 1). In Fig. 3 a negative value of ε suggests that precipitation might be too small, energy flux divergence might be too large, radiative cooling in the atmosphere might be too large, and/or downward surface sensible heat flux might be too large (i.e., the upward flux is too small). Global annual mean values are shown in Table 1, and zonal annual mean values are shown in Fig. 5. Figure 5 shows that the absolute value of the residual is larger over tropics, where precipitation and divergence of dry static and kinetic energy are large and atmospheric cooling is small. The annual mean divergence of dry static energy averaged over ocean is small. The net dry static energy transport occurs from land to ocean (not shown), which agrees with the result of Trenberth and Fasullo (2013). Global annual mean atmospheric shortwave and longwave irradiance and surface sensible heat flux agree with those given by Wild et al. (2015) to within their uncertainty.

Uncertainty estimates

The uncertainty in irradiances or precipitation rates is often expressed relative to observed values. Therefore, a large ε can be a result of a systematic relative bias. To investigate whether or not large biases shown in Fig. 3 are caused by a constant relative bias, we compare ε with the sum of uncertainties from the energy terms that appear in Eq. (1).

The uncertainty in the TOA shortwave and longwave irradiances are 1% ($k = 1$ or 1σ) and 0.8%, respectively, which are primarily caused by instrument calibration uncertainty (Loeb et al. 2009). The uncertainty in retrieved cloud properties contributes most to the uncertainty in surface shortwave irradiances (Kato et al. 2013). Uncertainties in near-surface temperature and precipitable water are two large contributors to the uncertainty in surface longwave irradiances (Zhang et al. 2006; Kato et al. 2013). Uncertainties in monthly gridded and annual global surface irradiances given by Kato et al. (2013) are nearly equivalent. We therefore take the uncertainty in the annual global mean surface irradiance and assume that errors in the upward and downward irradiances are uncorrelated in shortwave. This provides the upper limit of the net shortwave uncertainty if the errors in the upward and downward irradiances are positively correlated. For longwave we assume that errors in the upward and downward irradiances are correlated because the error in the skin temperature is likely to be correlated with the error in near-surface air temperature. The uncertainty (1σ) in the net surface shortwave and longwave irradiance over ocean is the sum of upward and downward uncertainties divided by the sum of upward and downward irradiance of global mean values over ocean [values in $\mathrm{W\,m^{-2}}$ are taken from Table 5 of Kato et al.

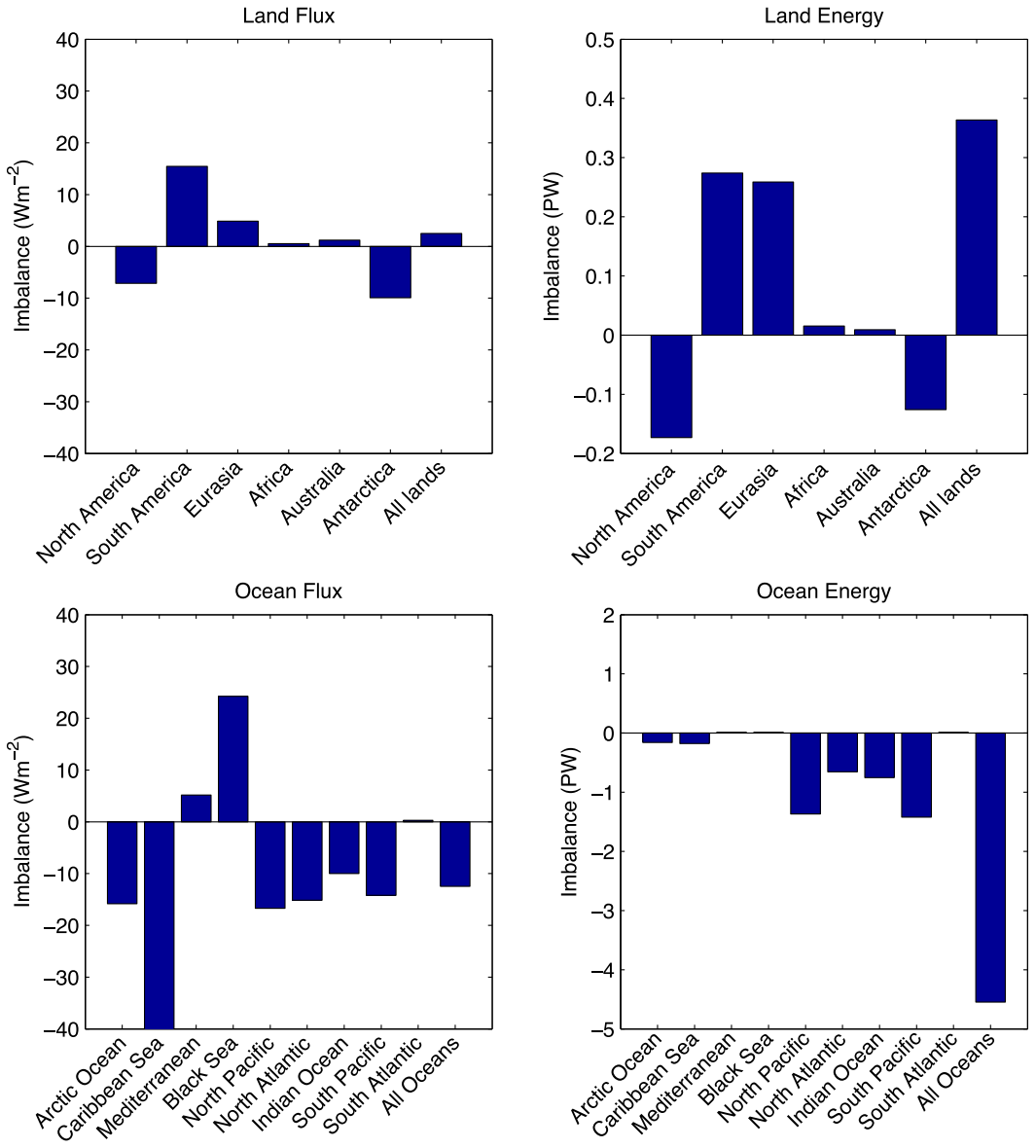

FIG. 2. (top) Column-integrated monthly mean atmospheric energy-budget residuals ε computed by Eq. (2) averaged over 10 years (March 2000 through February 2010) in (left) flux units and (right) energy units over land. The latter is the former multiplied by the respective area. Separation of regions follows that given by L'Ecuyer et al. (2015). (bottom) As in (top), but residuals are computed over ocean.

(2013)]; that is, $(4^2 + 3^2)^{1/2}/(190 - 12) = 0.028$ (2.8%) for shortwave and $(7^2 + 5^2 - 2r7 \times 5)^{1/2}/(402 - 354) = 0.051$ (5.1%) for longwave, where r is the correlation coefficient between upward and downward longwave irradiances. We use $r = 0.97$, which is the correlation coefficient between monthly mean upward and downward longwave irradiances over ocean (the correlation coefficient for global ocean plus land is 0.99) derived from CERES data. If all TOA and surface longwave and shortwave net irradiance errors are independent, the relative error in the net atmospheric irradiance is $(1^2 + 0.8^2 + 2.8^2 + 5.1^2)^{1/2} \approx 6\%$.

There are multiple sources of uncertainty for precipitation derived from space (Wolff and Fisher 2008; Stephens and Kummerow 2007) including sensor resolution, upper and lower thresholds of detection (that vary from ocean to atmosphere), temporal sampling, and blending different measurements from microwave, radar, and infrared. In addition, larger uncertainties are associated with heavy precipitation (e.g., Adler et al. 2012), drizzle (Berg et al. 2010; Adler et al. 2012), and snow (Behrangi et al. 2014). Adler et al. (2012) estimate the bias error in the global precipitation to be about

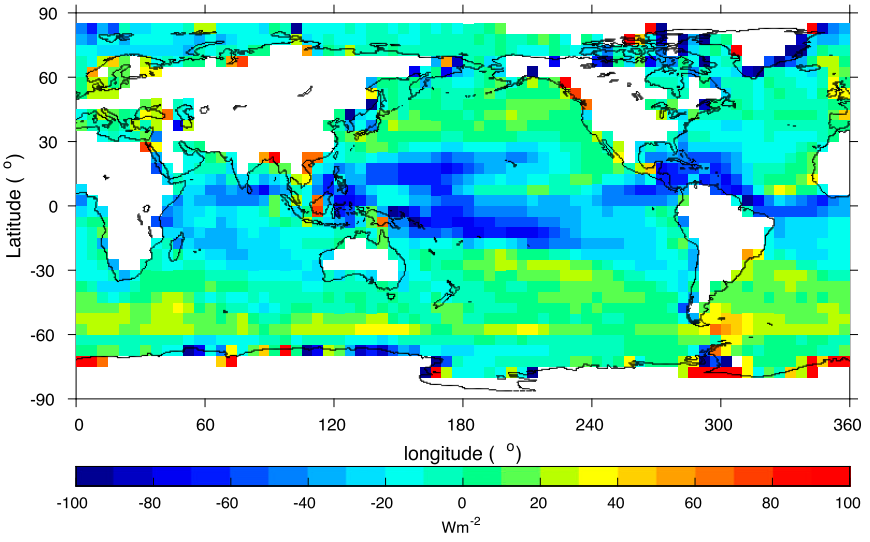

FIG. 3. Column-integrated monthly mean atmospheric energy-budget residual ε (W m^{-2}) computed by Eq. (2) averaged over 10 years from March 2000 through February 2010 in 5° × 5° grids.

7%–9%. Adler et al. (2012) also indicate that the bias error over the eastern Pacific and western Pacific can be as large as 20% and 10%–15%, respectively.

Estimating the bias error in atmospheric energy transport is more difficult because it depends on spatial scales. Mayer and Haimberger (2012) compute RMS difference of the monthly mean column-integrated divergence of atmospheric total energy from ERA-Interim and ERA-40. The RMS difference is about 40 W m^{-2} with a 125-km horizontal resolution. Because one 5° × 5° (500 km × 500 km) region contains sixteen 125 km × 125 km regions, we divide 40 W m^{-2} by the square root of 16. This assumes that errors over 16 regions are independent. The error of 10 W m^{-2} over a 5° × 5° region is a conservative estimate for two reasons. 1) Mayer and Haimberger (2012) use the difference between ERA-40 and ERA-Interim to estimate the 40 W m^{-2} error. Divergence from ERA-40 has known problems in the tropics (Trenberth et al. 2007). Therefore, using the difference of ERA-40 and ERA-Interim overestimates the error in ERA-Interim. 2) The error in divergence over 1° × 1° regions partially cancel in spatial averaging because the dry static energy divergence error is expected to be spatially anticorrelated (e.g., a positive divergence error tends to be present next to a negative divergence error), especially outside heavy precipitation regions. In addition, the power spectrum of the dry static energy divergence is ''blue''—that is, most power is at high spatial scales (Trenberth and Solomon 1993). Furthermore, the divergence error decreases faster than the error in atmospheric irradiance and precipitation in spatial averaging processes because both the global mean divergence and its error is exactly 0, while the error in other global mean flux components are not 0.

We divide 10 W m^{-2} by the mean of the absolute value of 5° × 5° dry static energy divergence over tropics of 67 W m^{-2} and use a 15% relative error for the sum of dry static and kinetic energy divergence. The RMS difference that Mayer and Haimberger (2012) compute is for the divergence of moist static energy plus kinetic energy. We are using the RMS difference for the divergence of dry static and kinetic energy. In the tropics and subtropics, moisture convergence gives rise to precipitation,

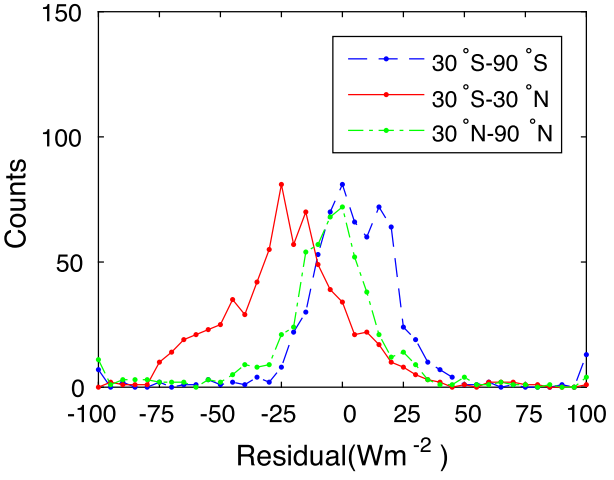

FIG. 4. Distribution of atmospheric energy-budget residual ε computed by Eq. (2) over 5° × 5° grid boxes shown in Fig. 3.

TABLE 1. Various forms of global annual mean energy fluxes and the residual over ocean computed using data from March 2000 through February 2010. (Sensible heat flux is averaged from January 2000 through December 2007.)

	Energy flux ($W m^{-2}$)[a]
Atmospheric shortwave irradiance	79
Atmospheric longwave irradiance	−194
Surface sensible heat flux	−17
Precipitation (*LP*)	83
Dry static energy divergence	−1
Kinetic energy divergence	−1
Residual	−12

[a] Over the global ocean, $1 W m^{-2}$ = 0.372 PW (Fasullo and Trenberth 2008).

resulting in dry static energy divergence (Trenberth and Stepaniak 2003a,b). Because of this cancellation, the moist static energy divergence is much smaller than that for the dry static energy, but the uncertainty is likely to be similar because it arises mainly from the divergence field itself. Hence, 15% of dry static energy divergence over the intertropical convergence zone, which is well over $30 W m^{-2}$, is likely an overestimate but could in part account for differences in using the result of Mayer and Haimberger (2012) for the uncertainty of dry static energy divergence. The uncertainty estimate of dry static energy divergence is more approximate than for irradiances and precipitation, and a rigorous estimate of dry static energy uncertainty needs further research.

To estimate the one-standard-deviation (1σ) envelope where the atmospheric energy balance resides, we assume that the 1σ uncertainty in the net atmospheric irradiance, precipitation, and dry static and kinetic energy divergence are 6%, 8%, and 15%, respectively. We also assume that all three bias errors with unknown sign are correlated, resulting in the upper limit of the 1σ envelope of $5° \times 5°$ gridded mean atmospheric net irradiance multiplied by 0.06 plus $5° \times 5°$ gridded precipitation multiplied by 0.08 plus $5° \times 5°$ gridded dry static energy divergence multiplied by 0.15. The left panel of Fig. 6 shows the 1σ envelope of the bias of the column-integrated monthly mean atmospheric energy in $5° \times 5°$ grids.

When we take the ratio of 1σ uncertainty (Fig. 6, left) to ε shown in Fig. 3, the ratio is not constant (Fig. 6, right). The ratio is generally larger than 1 over tropics (hence larger than the 1σ envelope), especially near regions with larger precipitation rate, larger dry static energy divergence, and less negative atmospheric net irradiance. Brown and Kummerow (2014), who investigated water mass balance, found a larger water imbalance than 8% over the tropical western Pacific. Our result indicates that large residuals (e.g., those over the central and western Pacific) are not part of a constant relative bias error of precipitation and radiation but made up by regionally dependent bias errors. If ε relative to the 1σ envelope is regionally dependent, we expect that residuals are associated with specific cloud types or weather systems. In the next section, we investigate what cloud types are likely associated with large residuals over the central and western Pacific.

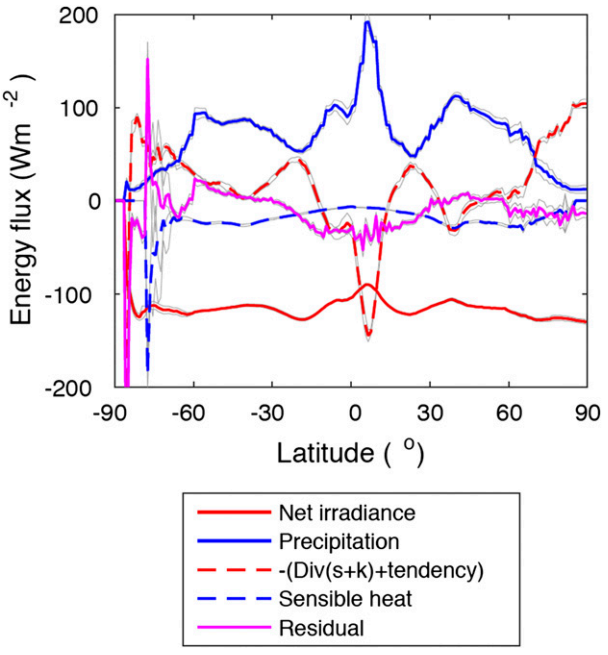

FIG. 5. Zonal annual mean column-integrated atmospheric energy component computed over the period from March 2000 through February 2010 (January 2000 through December 2007 for the sensible heat flux). Net irradiance and sensible heat flux is positive downward. The residual is the sum of all four terms. Thin gray lines indicate plus or minus one standard deviation of annual means over 10 years (7 yr for sensible heat flux).

5. Discussion

Figure 3 indicates that large negative residuals exist over the tropics. In addition, Fig. 6 implies that the residuals are not likely caused by a constant relative bias error. One way to understand the reason for the residual ε is to investigate cloud systems associated with ε because the precipitation rate and atmospheric net irradiance as well as the retrieval error in them depend on cloud type. In addition, large-scale dynamics also influences frequency of occurrence of specific cloud types. A study by Oreopoulos et al. (2014) shows that about 30% of clouds over the tropical western and central Pacific belong to cloud regime 2 (CR2) in which optically thick high clouds are present. Among cloud regimes defined by Oreopoulos et al. (2014), it is clear

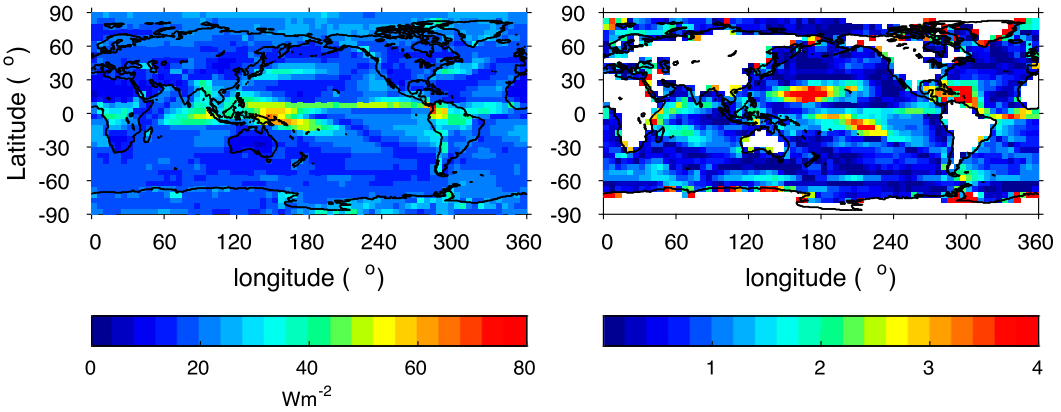

FIG. 6. (left) Monthly mean atmospheric energy bias error (1σ) over $5° \times 5°$ grids. Bias errors are the sum of 6% relative error in the net atmospheric irradiance, 8% relative error in the precipitation rate, and 15% relative error in the divergence term. (right) Atmospheric energy residual shown by Fig. 3 divided by the 1σ bias error envelope shown in (left).

that CR2 is the dominant cloud regime present over the tropical western and central Pacific. According to cloud types derived from *CloudSat* data (CLDCLASS; Sassen and Wang 2008), the dominant cloud type in CR2 is cirrus followed by stratocumulus, which together account for more than 50% of clouds (Oreopoulos et al. 2014). Deep convective clouds in CR2 account for less than 10% of all clouds, although deep convective clouds occur in this cloud regime more than any other regimes except for CR1 (Oreopoulos et al. 2014).

Cloud objects

To further identify which cloud types are associated with the negative residual over the tropical western Pacific, we utilize cloud objects derived from instantaneous observations by MODIS on *Aqua* (Xu et al. 2005, 2016a). A cloud object is defined as a contiguous region with similar cloud physical properties. Cloud fraction, cloud-top height, and optical thickness derived from MODIS over a CERES footprint are used to determine the cloud-object type (Table 2). Footprints containing the same cloud-object type are clustered and form a cloud object. The classification of cloud objects utilizes the shape and size of the cloud object using the cloud-system selection criteria (Wielicki and Welch 1986). Table 2 lists cloud-object types and selection criteria. Cloud objects are derived using only daytime observations (*Aqua* overpass time), but all CERES footprints from *Aqua* with a zenith viewing angle less than 48° are used. Note that cloud objects include clear sky that is present within a CERES footprint when the cloud fraction is less than 1 (fourth column of Table 2). Figure 3 of Xu et al. (2016a) shows the frequency of occurrence of cloud objects between 40°S and 40°N where all cloud objects are derived. Only deep convective cloud objects are derived from observations between 25°S and 25°N.

To identify cloud-object types present over regions with a large energy-budget residual, we compute the spatial correlation between the number of cloud objects

TABLE 2. Cloud-object type and selection criteria. Cloud objects are derived using only daytime data. Note that 440- and 680-hPa pressure levels are approximately 7 and 3.4 km, respectively above the sea level in the tropics.

Cloud-object type[a]	Cloud-top height	Cloud optical depth	Cloud fraction	Latitude band
Tropical deep convection	$h < 440$ hPa	>10	1.0	25°S–25°N
Trade/shallow cumulus	$h > 680$ hPa	—	0.1–0.4	40°N–40°S
Transition stratocumulus	$h > 680$ hPa	—	0.4–0.99	40°N–40°S
Solid stratus	$h > 680$ hPa	—	0.99–1.0	40°N–40°S
Altocumulus	$440 < h < 680$ hPa	—	0.1–0.4	40°N–40°S
Transition altocumulus	$440 < h < 680$ hPa	—	0.4–0.99	40°N–40°S
Solid altocumulus	$440 < h < 680$ hPa	—	0.99–1.0	40°N–40°S
Cirrus	$h < 440$ hPa	<10	0.1–0.4	40°N–40°S
Cirrocumulus	$h < 440$ hPa	<10	0.4–0.99	40°N–40°S
Cirrostratus	$h < 440$ hPa	<10	0.99–1.0	40°N–40°S

[a] All cloud objects of given type are grouped into three size categories, 100–150 km, 150–300 km, and greater than 300 km.

TABLE 3. Spatial correlation of 5° × 5° areas of the number of cloud objects and residual ε in column-integrated atmospheric energy. Correlation coefficients are computed using between 40°S and 40°N (25°S and 25°N for deep convective clouds; the number of ocean grid boxes are 599 between 25°S and 25°N and 943 between 40°S and 40°N) averaged from July 2006 through June 2010 (January 2000 through June 2010 for deep convective clouds). The uncertainty in correlation coefficients is determined by 1000 bootstrap computations.

Cloud-object type	Correlation coefficient	Fractional area covered by cloud objects[a]
Shallow cumulus	0.41 ± 0.03	0.07
Stratocumulus	−0.11 ± 0.02	0.07
Stratus	−0.24 ± 0.02	0.03
Altocumulus	−0.36 ± 0.03	0.00
Cirrus	−0.10 ± 0.03	0.00
Cirrocumulus	0.02 ± 0.03	0.00
Cirrostratus	0.13 ± 0.03	0.03
Deep convection	0.14 ± 0.04	0.03
Sum	—	0.24

[a] The number of footprints used for cloud objects (numbers over 4 years are taken from Table 3 of Xu et al. 2016a) divided by the number of daytime footprints with a zenith viewing angle less than 48° (~386 000 day^{-1}).

and atmospheric energy-budget residuals in 5° × 5° grids. Residuals are divided by regional mean values (between 25°S and 25°N for deep convective clouds and between 40°S and 40°N for other cloud objects). The spatial correlation coefficient is computed between the total number of a given cloud-object type for the entire period in each 5° × 5° grid box and the mean residual in the grid box over the period divided by the regional mean averaged over the period. Because residuals are generally negative, when they are divided by the regional mean that is also negative, cloud objects are associated with larger absolute values of the residual if the correlation coefficient is positive. Among eight cloud-object types, shallow cumulus, cirrostratus, and deep convective cloud types show a positive correlation (Table 3) that are significant at a 95% confidence level given by $1.96/N^{1/2}$, where N is the number of grid boxes ($N = 599$ for deep convective cloud objects and $N = 943$ for other cloud objects). The largest correlation coefficient is 0.41 with shallow cumulus cloud objects. In this spatial correlation computation, three cloud-object types—altocumulus, transition altocumulus, and solid altocumulus (listed in Table 2)—are grouped together in order to compute the spatial correlation coefficient. Also, all size categories of the cloud object (100–150 km, 150–300 km, and larger than 300 km) are grouped together. When all cloud objects listed in Table 3 are added, they account for about a half of clouds over the tropics (cloud fraction of 0.24 vs actual daytime cloud fraction of 0.56). Because cloud objects require a minimum 12 CERES footprints to form a cloud object, clouds clustered over an area with the size less than 75 km in diameter are likely to be missing. Even if we include all sizes, the spatial correlation coefficient is likely to be nearly equal because regions where specific cloud-object types occur are not altered.

Among three cloud-object types having a positive spatial correlation, large convective clouds of which size is greater than 300 km occur predominately over the central and western Pacific (Xu et al. 2016a). Large convective clouds are about 25% of the total number of convective cloud objects and account for about 76% of the area covered by convective cloud objects. Regions with large convective clouds are associated with the intertropical convergence zone (ITCZ). The ITCZ location depends on season and is in the summer hemisphere. Regions with a large negative residual also change by season and coincide with regions with large deep convective clouds (Fig. 7). Figure 7 also reveals that regions with a large negative residual extend farther east than regions with large deep convective clouds. Often shallow cumulus clouds are present over this region (Fig. 8). Shallow cumulus over this region also tend to cover a large area with linear dimension larger than 300 km. Note that the cloud fraction of shallow cumulus clouds over a CERES footprint of approximately 20 km in size is 0.4 or less. These results suggest that even though spatial correlation of single cloud objects is low, areas covered by either deep convective clouds or shallow cumulus are spatially correlated with regions with ε.

To further diagnose what cloud-object types are associated with residuals of the atmospheric energy budget, which might suggest the energy-budget component with a large bias error, we analyze the temporal correlation of ε averaged over a month divided by the mean ε over the entire period and the number of cloud objects present in a month. Similar to the spatial correlation, a positive correlation indicates that the absolute value of ε increases with increasing the number of cloud objects. For the temporal correlation, we only use the sum of the net atmospheric irradiance, precipitation, and dry static and kinetic energy divergence and their tendencies, which corresponds to the sum of the residual ε and (positive downward) surface sensible heat flux [hereinafter $R + LP - \nabla \cdot \mathbf{U}\,(s + k) - \partial(s + k)/\partial t = \varepsilon + F_{\mathrm{sh}}$] because 1) no surface sensible heat flux from SeaFlux is available after December 2007 and 2) the uncertainty in monthly mean regional sensible heat fluxes can be very large. In addition, we only analyze the correlation coefficient between the number of cloud objects in a month and the monthly mean atmospheric energy-budget residual. Therefore, as long as the contribution from the

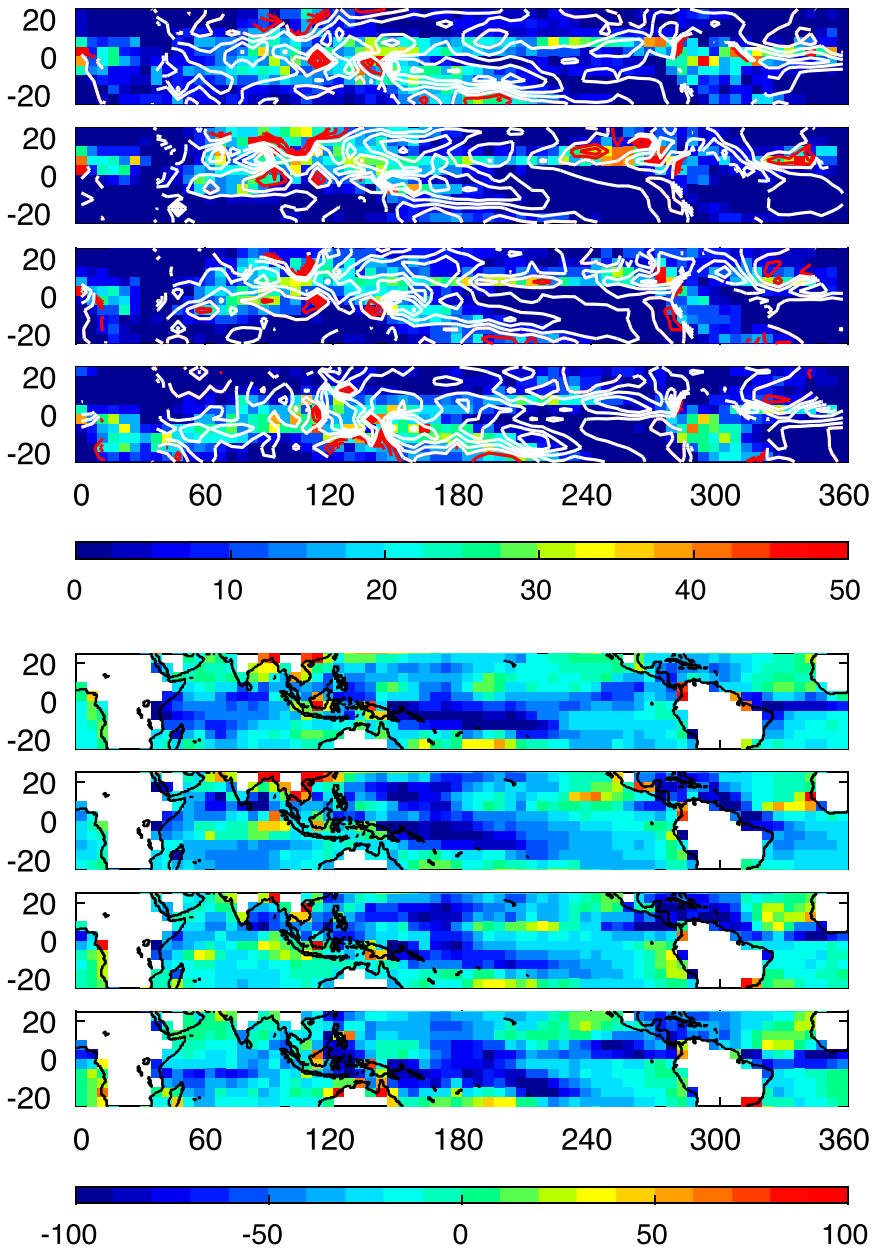

FIG. 7. (top) The number of deep convective cloud objects of which extends larger than 300 km over 54 months from January 2006 through June 2010 in color for March–May, June–August, September–November, and December–February. (bottom) The corresponding atmospheric energy-budget residual over the ocean ($W m^{-2}$). Contours in (top) indicate the atmospheric energy-budget residual over the ocean from (bottom), with red contours for positive values and white contours for negative values.

surface sensible heat flux to the atmospheric energy variability is small, neglecting the surface sensible heat flux does not affect the correlation coefficient very much. Note that the annual mean value of $\varepsilon + F_{sh}$ is from -20 to $-30\,W m^{-2}$ with the standard deviation of monthly values of about $10\,W m^{-2}$ over the tropical Pacific, while the annual mean of the sensible heat flux is about $-10\,W m^{-2}$ with the standard deviation of monthly mean values of 2–3 $W m^{-2}$ except over the southwestern Pacific. The standard deviation of monthly mean sensible heat flux over the southwestern Pacific is about $6\,W m^{-2}$.

We separate the Pacific region into four subregions—the southwestern Pacific, northwestern Pacific, southeastern

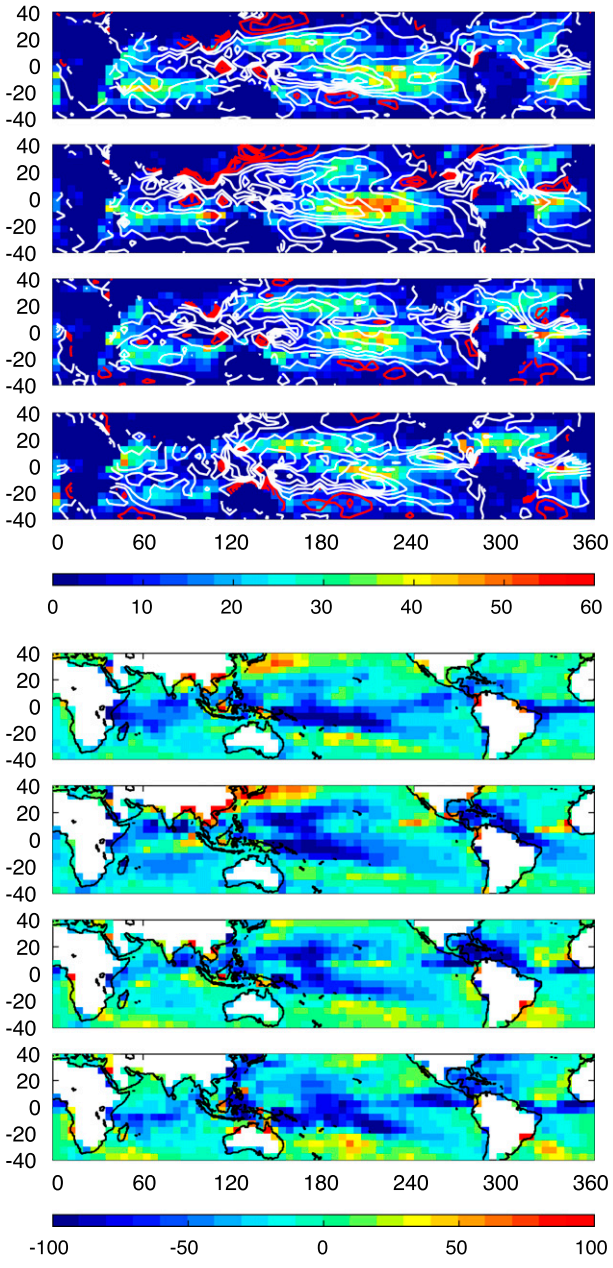

FIG. 8. (top) The number of shallow cumulus cloud objects of which extends larger than 300 km over 48 months from July 2006 through June 2010 in color for March–May, June–August, September–November, and December–February. (bottom) The corresponding atmospheric energy-budget residual over the ocean ($W m^{-2}$). Contours in (top) indicate the atmospheric energy-budget residual over the ocean from (bottom), with red contours for positive values and white contours for negative values.

Pacific, and northeastern Pacific—to make the seasonal variation of deep convective and shallow cumulus cloud-object types in each subregion distinct. We first compute the correlation coefficient with net atmospheric irradiance, precipitation, and divergence (plus tendency term) separately with the number of deep convective cloud objects. All net atmospheric irradiance, precipitation, and divergence are correlated well with the number of deep convective clouds with a better correlation with large (>300 km) deep convective cloud objects (Table 4). Positive correlation coefficients for precipitation, divergence, and atmospheric net irradiance are expected because deep convective clouds are a large source of precipitation and they make the net atmospheric irradiance less negative. The atmosphere is warmed by latent heat release and radiative effect of deep convective clouds. Dynamics transports the energy vertically and exports the energy from these regions (Riehl and Malkus 1958). Figure 9 (top) shows the monthly mean number of deep convective cloud objects divided by the annual mean number of cloud objects by solid blue lines. Red lines are monthly mean values of atmospheric net irradiance, precipitation rate, and dry static and kinetic energy divergence plus their tendencies divided by respective annual mean values. The shape of the normalized seasonal variability of the occurrence of deep convective clouds and precipitation rate is nearly identical. Note that the net atmospheric irradiance is negative so that it is less negative in months with a larger number of deep convective cloud objects. The top panels of Fig. 9 show that for the southern and northern tropical western Pacific regions, the seasonal variation of net atmospheric irradiance, precipitation, and divergence are primarily driven by the seasonal variation of deep convective cloud-object occurrence.

Second, we correlate the sum of three energy components, which equals $\varepsilon + F_{sh}$, divided by the annual mean of $\varepsilon + F_{sh}$ with monthly occurrence of three cloud-object types separately that are present over four tropical Pacific regions. The size of cloud-object types used for the temporal correlation is larger than 300 km for deep convective cloud and shallow cumulus and between 100 and 150 km for cirrostratus because of a small number of occurrences of cirrostratus cloud objects greater than 300 km. All three energy components are added; $\varepsilon + F_{sh}$ is nearly constant (negative) throughout a year (Fig. 9, bottom). As a result, deep convective cloud-object occurrence is negatively correlated with $\varepsilon + F_{sh}$, or the correlation is not statistically significant. This indicates that ε is not likely associated with all deep convective clouds equally. If ε is associated with deep convective clouds, the error-estimating energy components associated with deep convective clouds must vary depending on the individual deep convective cloud. However, $\varepsilon + F_{sh}$ appears to be positively correlated with occurrence of shallow cumulus cloud objects over all four tropical Pacific regions (Fig. 10). The correlation coefficient between shallow cumulus and $\varepsilon + F_{sh}$ is

TABLE 4. Temporal correlation coefficient between monthly mean net atmospheric irradiance, precipitation rate, or sum of dry static and kinetic energy divergence and tendency and the monthly number of deep connective cloud objects of which size is (first number) 100–150 km, (second number) 150–300 km, and (third number) greater than 300 km over two tropical regions. Numbers in parentheses are annual mean values of net atmospheric irradiance, precipitation multiplied by the latent heat of vaporization, and the sum of dry static and kinetic energy divergence and their tendency (W m^{-2}).

Region	Lat	Lon	Net atmospheric irradiance	Precipitation	Divergence plus tendency
Southwestern Pacific[a]	0°–25°S	105°E–180°	0.75/0.75/0.81 (−94.4)	0.86/0.86/0.96 (128.6)	0.87/0.87/0.93 (78.2)
Northwestern Pacific[a]	0°–25°N	105°E–180°	0.83/0.82/0.86 (−98.4)	0.82/0.84/0.93 (144.9)	0.86/0.86/0.92 (92.4)
Southeastern Pacific	0°–25°S	75°W–180°	0.80/0.70/0.82 (−126.2)	0.68/0.60/0.83 (54.1)	0.85/0.80/0.92 (–30.7)
Northeastern Pacific	0°–25°N	75°W–180°	0.68/0.73/0.57 (−111.8)	0.82/0.80/0.92 (104.8)	0.86/0.86/0.95 (33.2)

[a] Regions include eastern Indian Ocean.

greater than 0.5 over the northwestern Pacific and southeastern Pacific as well as over inter-American seas (Table 5). Both are greater than a 95% confidence level of 0.28. Even though shallow cumulus cloud objects include clear-sky areas, a weak correlation between clear-sky area and $\varepsilon + F_{sh}$ for all regions suggests that the presence of shallow cumulus is needed for large correlations. In addition, the correlation coefficients of shallow cumulus clouds for all regions are larger than the standard deviation estimated by 1000 bootstrap

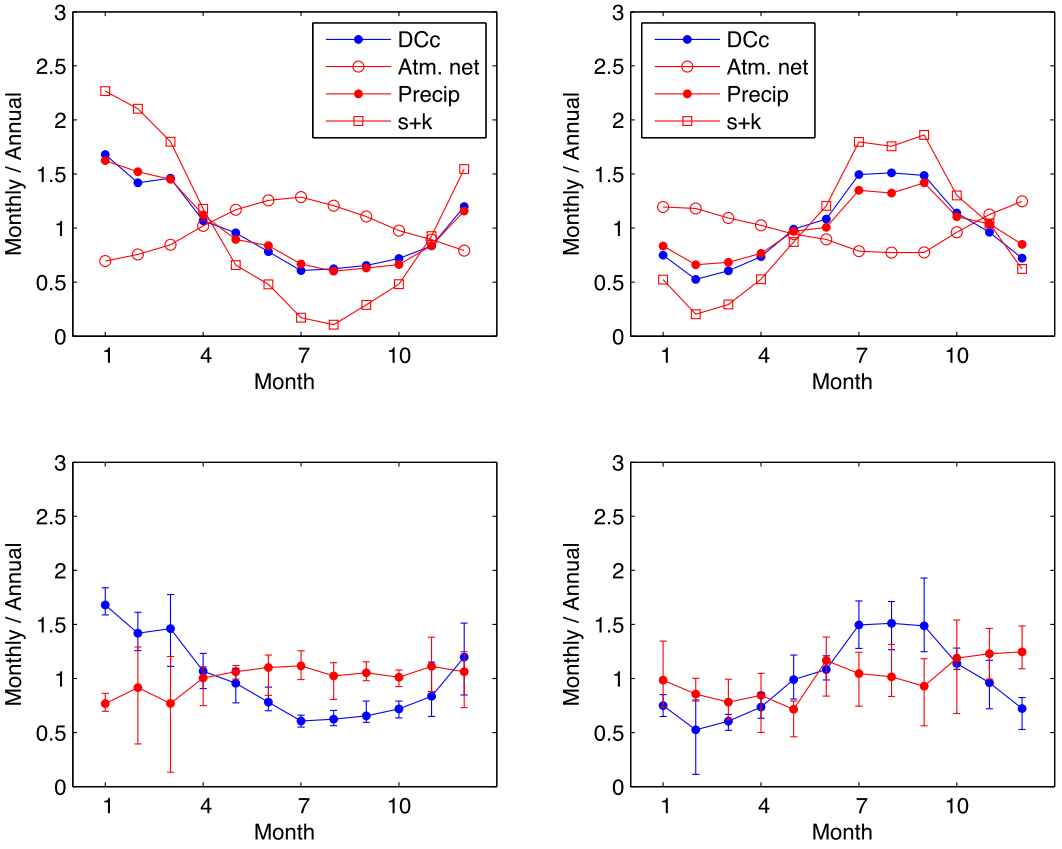

FIG. 9. (top) Monthly mean value divided by the annual mean value for number of large (>300 km) deep convective cloud objects in a month (blue line), net atmospheric irradiance (red line with circles), precipitation rate (red line with filled circles), and dry static and kinetic energy divergence and tendency (red line with squares). (bottom) The sum of monthly mean net atmospheric irradiance, precipitation multiplied by the latent heat of vaporization, and dry static and kinetic energy divergence and tendency, which equals $\varepsilon + F_{sh}$ divided by the annual mean value (red line), and the blue line is as in (top). Shown are values for the (left) southwestern Pacific (0°–25°S, 105°E–180°) and (right) northwestern Pacific (0°–25°N, 105°E–180°). Data taken from January 2006 through June 2010 are used. Error bars in (bottom) indicate maximum and minimum values over the period.

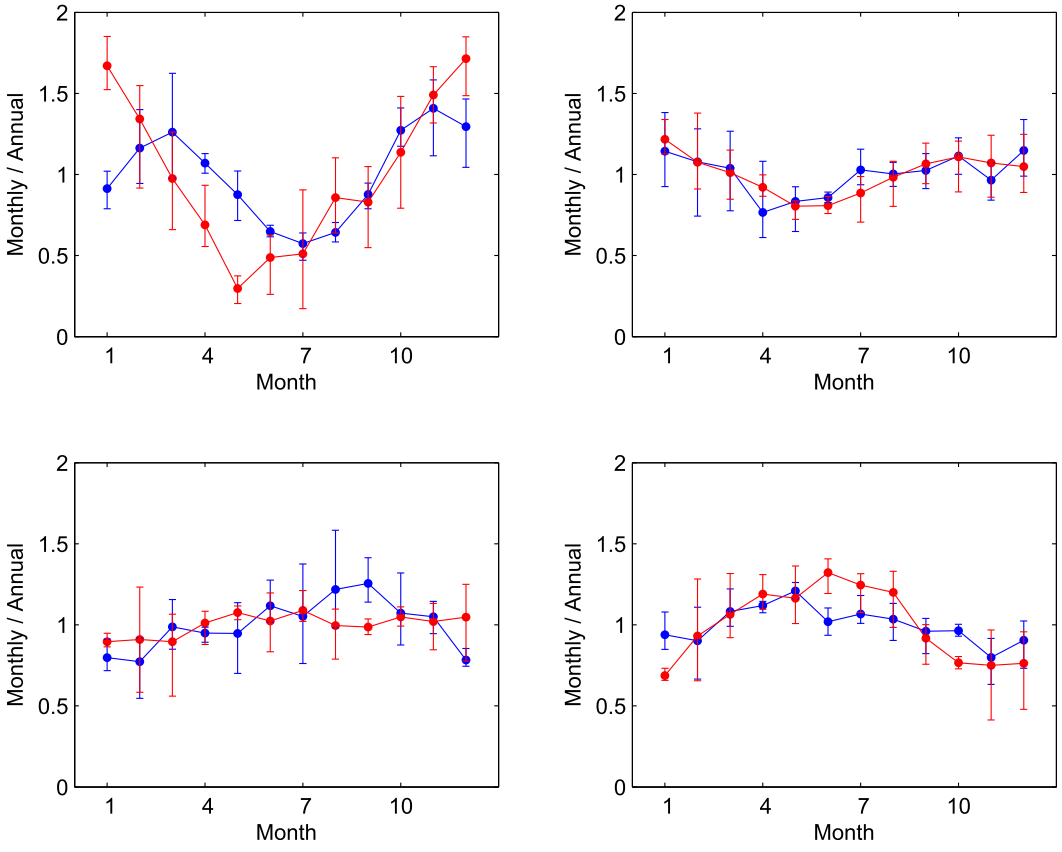

FIG. 10. Monthly mean value divided by the annual mean value for number of large (>300 km) shallow cumulus cloud objects in a month (blue line) and the sum of monthly mean net atmospheric irradiance, precipitation multiplied by the latent heat of vaporization, and dry static and kinetic energy divergence and tendency, which equals $\varepsilon + F_{sh}$ divided by the annual mean value (red line) for the (top left) northwestern Pacific (0°–40°N, 105°E–180°), (top right) northeastern Pacific (0°–40°N, 75°W–180°), (bottom left) southwestern Pacific (0°–40°S, 105°E–180°), and (bottom right) southeastern Pacific (0°–40°N, 75°W–180°). Data taken from July 2006 through June 2010 are used. Error bars indicate maximum and minimum values over the period.

computations (e.g., Wilks 1995). For the bootstrap computations, we sample the pair of $\varepsilon + F_{sh}$ and number of cloud objects in a month n times, where n is the number of months in the time series. We then compute the correlation coefficient. We repeat this 1000 times. The uncertainty in the correlation coefficient is given by the standard deviation of the distribution. If autocorrelation of the time series is considered, the uncertainty increases approximately by a factor of 2. The correlation coefficient between $\varepsilon + F_{sh}$ and shallow cumulus cloud occurrence over the southwestern Pacific is smaller than a 95% confidence level while deep convective cloud occurrence is negatively correlated. It is possible that higher clouds such as deep convective clouds mask shallow cumulus clouds over the southwestern Pacific. However, that should be true for the northeastern Pacific, and the difference between these two regions affecting the correlation coefficient is not clear. A further study is left for the future.

In Figs. 9 and 10, monthly mean values are normalized by their respective annual mean. The correlation coefficient does not change even if monthly means are not normalized by the annual mean except the sign of the coefficient. A question remains, however, if shallow cumulus clouds alter atmospheric energy fluxes very little, even if the correlation coefficient is large, whether or not they can account for the energy-budget residual. A study by Berg et al. (2010) shows that the precipitation rate over the tropical eastern Pacific estimated from the *CloudSat* radar that is not included in the estimate from the TRMM radar is about 0.4–0.5 mm day^{-1}, which is approximately 13 W m^{-2}, although the 150-km-radius range over Barbuda area-averaged precipitation rate by shallow cumuli estimated by Nuijens et al. (2009) reaches about 35 W m^{-2}. Kato (2009) shows that the atmospheric cooling by clouds with the top pressure height greater than 665 hPa is from 0 to −25 W m^{-2} over the tropics. According to Oreopoulos et al. (2014) low-level

TABLE 5. Temporal correlation coefficient between $\varepsilon + F_{sh}$ and the number of cloud objects in a month. The uncertainty of the correlation coefficient is determined by 1000 bootstrap computations. Numbers in parentheses are the average number of cloud objects in a 5° × 5° grid in a month. Observations from January 2006 through June 2010 (54 months) for deep convective cloud objects (DC) and from July 2006 through June 2010 (48 months) for other objects are used.

Region	Lat	Lon	Shallow cumulus (size > 300 km)	Cirrostratus (150 > size > 100 km)	Deep convective (size > 300 km)	Clear-sky area[a]
Southwestern Pacific[b]	0°–40°S (0°–25°S for DC)	105°E–180°	0.20 ± 0.15 (0.52)	−0.34 ± 0.13 (3.91)	−0.65 ± 0.10 (0.96)	−0.07 ± 0.11
Northwestern Pacific[b]	0°–40°N (0°–25°N for DC)	105°E–180°	0.52 ± 0.09 (0.76)	−0.54 ± 0.08 (4.35)	0.13 ± 0.12 (1.03)	0.12 ± 0.13
Southeastern Pacific	0°–40°S (0°–25°S for DC)	75°W–180°	0.63 ± 0.08 (1.14)	−0.14 ± 0.12 (2.08)	−0.05 ± 0.15 (0.36)	−0.13 ± 0.13
Northeastern Pacific	0°–40°N (0°–25°N for DC)	75°W–180°	0.32 ± 0.14 (0.83)	−0.28 ± 0.14 (3.14)	−0.31 ± 0.11 (0.75)	−0.10 ± 0.14
Inter-American seas	0°–40°N (0°–25°N for DC)	45°–90°W	0.67 ± 0.07 (1.11)	−0.30 ± 0.11 (3.51)	0.07 ± 0.12 (0.69)	−0.10 ± 0.13

[a] Clear-sky fraction is derived from MODIS on *Aqua* using daytime observations.
[b] Regions include eastern Indian Ocean.

clouds account for roughly 50% of clouds present in cloud regime 2. These lead to about a 10 W m^{-2} contribution to atmospheric cooling by shallow cumuli. The sensible heat flux is about −10 W m^{-2} (positive downward) over the tropical western Pacific. Therefore, unless the error in estimating energy components from satellite observations for shallow cumulus clouds is very large, it appears that the residual of 50 W m^{-2} is too large to close by shallow cumulus alone. It is possible that both the atmospheric energy-budget residual and the number of shallow cumulus cloud objects are caused by something else through teleconnections so that the correlation between them is good.

A study by Neggers et al. (2007) suggests that shallow cumuli affect the width and strength of ITCZ and atmospheric energy budget by a mechanism termed the shallow cumulus humidity throttle. Shallow cumulus clouds over the tropics affect vertical transport of water vapor and increase humidity in the free troposphere. A more humid free troposphere leads to a broader ITCZ and more precipitation by deep convective clouds (Neggers et al. 2007). A reduction in the mixing time scale of shallow convection leads to a more humid mixing layer, a dryer free troposphere, a narrower ITCZ, stronger large-scale convergence, and more intense convection (Neggers et al. 2007). A study by Xu et al. (2016, manuscript submitted to *J. Quant. Spectrosc. Radiat. Transfer*) also shows that a larger number of shallow cumulus cloud objects is associated with a smaller size of deep convective clouds. One possibility is that more intense precipitation within the ITCZ is not detected by satellite instruments. However, a small spatial correlation coefficient with deep convective cloud objects implies that this may not be the only process affecting the residual. Nevertheless, energy budgets derived from satellite observations need to be improved at least to a level that observations can be used to determine whether or not the mechanism exists.

Even if shallow cumulus and deep convective cloud objects are not connected with the shallow cumulus humidity throttle, these two cloud objects can be related energetically. The surface latent heat flux over shallow cumulus regions is about 160 W m^{-2} (Nuijens et al. 2009), while the shallow cumulus precipitation rate is about 35 W m^{-2} (Nuijens et al. 2009). Therefore, most water vapor entering the atmosphere from the ocean over shallow cumulus regions is exported from the regions and precipitated by other cloud-object types. Because regions with large energy-balance residual appear to be present encompassing both regions with shallow cumulus and deep convective cloud objects, it is possible that missing an energetic link due to water vapor between these two cloud objects in satellite observations contributes to the energy-budget-balance residual. In addition, spatial and temporal mismatch of dry static divergence resulting from poor representations of shallow cumulus in reanalysis can cause a regional energy-budget residual. If, however, the error in the dry static energy divergence contributes significantly to local energy-budget residuals, the cause of local residuals and global residual are different because the error in the dry static energy divergence is 0, if it is integrated over the globe. It is also possible that cumulus congestus are sometimes present under cirrostratus (see the supplemental material). These overlapping cloud objects are not included in this study. If these cloud-object-type occurrences are not correlated, the probability of overlapping two cloud objects are the product of each cloud-object occurrence (i.e., random overlap). Therefore, the overlapping probability is about one order magnitude smaller than each

cloud-object occurrence. This gives a smaller radiative impact of cumulus congestus under cirrostratus, but precipitation by cumulus congestus could be significant (Chen and Liu 2016).

Results presented here perhaps underscore the complexity of understanding the cause of energy-budget residual that is a result of partial cancelation of three large components. Even though individual components are reasonable in producing seasonal variations and correlation to cloud types, a significant residual remains once all components are added. To move forward, the results suggest the importance of understanding processes associated with energy flow and the link among components.

6. Conclusions

We investigated regions where a large residual in column-integrated atmospheric energy occurs using Ed2.8 of CERES EBAF products for net atmospheric irradiances, GPCP V2.2 for precipitation, SeaFlux version 1 for surface sensible heat flux, and ERA-Interim for dry static and kinetic energy divergence and tendency. The residuals of atmospheric energy primarily occur over ocean and the value varies spatially. The residual tends to be negative over the tropics and positive over midlatitudes. A negative residual indicates that precipitation might be too small, divergence might be too large (convergence too small), radiative cooling might be too large, or upward sensible heat flux is too small. Negative residuals exceeding $-50\,\mathrm{W\,m^{-2}}$ are present over the tropical western Pacific. The residual is larger than the sum of constant relative errors in precipitation (8%), radiative cooling (6%), and divergence (15%) for most tropical regions, especially over the western and central Pacific. Regions with a large relative residual partly coincide with and farther extend outside of regions with large precipitation rate, large dry static energy divergence, and less negative net atmospheric irradiance.

The frequency of occurrence of shallow cumulus, cirrostratus, and deep convective cloud objects are spatially correlated with regions with a large negative residual. When the tropical Pacific is divided into four regions, temporal correlation coefficients between the number of deep convective cloud objects and individual components, net atmospheric irradiance, precipitation rate, and the sum of dry static and kinetic energy divergence and tendency over the western Pacific are 0.84, 0.95, and 0.93, respectively. The large correlation coefficient is caused primarily by the seasonal variation of deep convective cloud occurrence. The correlation coefficient is, however, either negative or statistically insignificant when it is computed between the number of deep convective cloud objects and the sum of monthly mean net atmospheric irradiance, precipitation rate multiplied by the latent heat of vaporization, and dry static and kinetic energy divergence and their tendency $\varepsilon + F_{\mathrm{sh}}$ divided by the annual mean. Instead, the number of shallow cumulus cloud objects correlates well over the tropical Pacific. These results suggest that 1) if retrieval errors associated with deep convective clouds are causing the column-integrated atmospheric energy-budget residual, the errors must vary among individual deep convective clouds; 2) even though the shallow cumulus cloud objects are temporally correlated with the residual, retrieval errors for shallow cumulus clouds are not likely to account for all of the residual because associated atmospheric energy fluxes are smaller than the residual; and 3) it is possible that the residual is associated with processes in which shallow cumulus clouds affect free-troposphere humidity and the precipitation by deep convective clouds and hence the atmospheric energy budget over the tropical western Pacific. Alternatively, processes affecting both the residual and occurrence of shallow cumulus clouds might exist.

If the shallow cumulus humidity throttle is responsible for a part of the residual, identifying the cause of the residual might be more elusive than when the residual is caused by a single cloud type. However, investigating the link between deep convective and shallow cumulus clouds might be the first step to understand the cause of atmospheric energy and surface-energy-budget residual.

Acknowledgments. We thank Dr. Louise Nuijens of MIT for useful discussions, Mr. Walter Miller for providing cloud fractional coverage by cloud objects, and three anonymous reviewers for providing constructive comments. The work was supported by the NASA CERES and NEWS projects. The research of K. E. Trenberth is partially sponsored by DOE Grant DE-SC0012711. T. J. Thorsen is supported by a NASA Postdoctoral Program Fellowship. The CERES datasets were obtained from the NASA CERES website (http://ceres.larc.nasa.gov/order_data.php), GPCP data were obtained from the NASA GSFC website (http://precip.gsfc.nasa.gov/), SeaFlux data were obtained online (http://seaflux.org/), and ERA-Interim data were obtained from NCAR (http://www.cgd.ucar.edu/cas/catalog/newbudgets/index.html#AtD).

APPENDIX

Atmospheric Energy Budget Equations

Derivation of column-integrated energy balance equations follows Vallis (2006), Trenberth (1997), and

Trenberth and Stepaniak (2003a). All equations derived here are not new but the purpose to derive vertically integrated atmospheric energy equations is to clarify assumptions made in the derivations.

The energy equation in the pressure coordinate is derived in a similar way as that in z coordinate. Because the surface pressure at the lower boundary changes temporally and spatially, however, energy equations given by Boer (1982) are needed to compute atmospheric energy in practice. Here we derive the atmospheric energy balance equation to clarify assumptions. Kinetic, internal, and potential energy equations per unit mass in pressure coordinate are

$$\frac{Dk}{Dt} = -\mathbf{U}\cdot\nabla_p\Phi - J_{\rm fr}, \tag{A1}$$

$$c_v\frac{DT}{Dt} + \frac{D(p\alpha)}{Dt} - \alpha\omega = J_{\rm rad} + J_{\rm lh} + J_{\rm sh} + J_{\rm fr}, \tag{A2}$$

and

$$\frac{D\Phi}{Dt} = gw, \tag{A3}$$

where $\mathbf{U}$ is the horizontal wind vector, $k = 1/2\mathbf{U}^2$, Φ is the geopotential, c_v is the specific heat of air at constant volume, T is air temperature, p is the pressure, α the specific volume of air, g is acceleration due to gravity, $\omega = Dp/Dt$, $w = Dz/Dt$, and $J_{\rm rad}$, $J_{\rm lh}$, $J_{\rm sh}$, and $J_{\rm fr}$ are diabatic heating due to radiation, latent heat, sensible heat, and friction (or frictional dissipation), respectively.

Because $\alpha\omega = (\partial\Phi/\partial t + \mathbf{U}\cdot\nabla_p\Phi) - D\Phi/Dt$, Eq. (A2) also relates w and ω, which gives

$$c_v\frac{DT}{Dt} + \frac{D(p\alpha)}{Dt} - \left(\frac{\partial\Phi}{\partial t} + \mathbf{U}\cdot\nabla_p\Phi - gw\right) = J_{\rm rad} + J_{\rm lh} + J_{\rm sh} + J_{\rm fr}. \tag{A4}$$

Adding Eqs. (A2) and (A3) leads to

$$c_p\frac{DT}{Dt} + \frac{D\Phi}{Dt} = \frac{\partial\Phi}{\partial t} + \mathbf{U}\cdot\nabla_p\Phi + J, \tag{A5}$$

where specific heat of air at constant pressure $c_p = c_v + p\alpha$ and $J = J_{\rm rad}+J_{\rm lh}+J_{\rm sh}$.

Because the integration from surface pressure to the top of atmosphere gives the mass of the atmosphere above the surface with geopotential Φ_s, and the surface pressure (i.e., mass) can change with time even though the surface geopotential is constant with time (i.e., $\partial\Phi_s/\partial t = 0$), Φ_s is added to the tendency term (Trenberth 1997). Therefore Eq. (A5) is written as follows:

$$\frac{\partial(c_pT+\Phi_s)}{\partial t} + \nabla_p\cdot[\mathbf{U}(c_pT+\Phi)] + \frac{\partial\omega(c_pT+\Phi)}{\partial p} = \mathbf{U}\cdot\nabla_p\Phi + J_{\rm rad} + J_{\rm lh} + J_{\rm sh} + J_{\rm fr}, \tag{A6}$$

which is equivalent to Eq. (20) of Boer (1982). The sum of kinetic, internal, and potential energy is

$$\frac{\partial(c_pT+\Phi_s+k)}{\partial t} + \nabla_p\cdot[\mathbf{U}(c_pT+\Phi+k)] + \frac{\partial\omega(c_pT+\Phi+k)}{\partial p} = J, \tag{A7}$$

where $J = J_{\rm rad} + J_{\rm lh} + J_{\rm sh}$ and continuity equation $\nabla_p\mathbf{U} + \partial\omega/\partial p = 0$ is used.

Equation (A7) is equivalent to Eq. (15) of Trenberth (1997) and Eq. (3b) of Trenberth and Smith (2009).

We integrate Eq. (A7) over the entire atmospheric column:

$$\frac{1}{g}\int_0^{p_s}\frac{\partial}{\partial t}(c_pT+\Phi_s+k)\,dp + \frac{1}{g}\int_0^{p_s}\nabla_p\cdot\mathbf{U}(c_pT+\Phi+k)\,dp + \frac{1}{g}\int_0^{p_s}\frac{\partial\omega(c_pT+\Phi+k)}{\partial p}dp = \frac{1}{g}\int_0^{p_s}J\,dp. \tag{A8}$$

Because

$$\int_0^{p_s}\frac{\partial\omega(c_pT+\Phi+k)}{\partial p}dp = \left(\frac{\partial p_s}{\partial t} + \mathbf{U}_s\cdot\nabla_p p_s\right)(c_pT_s+\Phi_s+k_s), \tag{A9}$$

the third term of the left-hand side of Eq. (A8) is canceled when the time and horizontal derivative are brought outside the integrals on the left-hand side of Eq. (A8):

$$\frac{1}{g}\frac{\partial}{\partial t}\int_0^{p_s}(c_pT+\Phi_s+k)\,dp + \frac{1}{g}\nabla_p\cdot\int_0^{p_s}\mathbf{U}(c_pT+\Phi+k)\,dp = \frac{1}{g}\int_0^{p_s}J\,dp. \tag{A10}$$

Equation (A10) is the atmospheric energy equation for a unit area and equivalent to Eq. (4) of Trenberth and Smith (2009). In Eq. (A10), $J = J_{\rm rad} + J_{\rm lh} + J_{\rm sh}$ and when it is integrated over the atmospheric column,

$$\frac{1}{g}\int_0^{p_s}J\,dp = \int_0^{\infty}\rho(J_{\rm rad}+J_{\rm lh}+J_{\rm sh})\,dz = (R_T - R_s) + L(P+C) - F_{\rm sh}, \tag{A11}$$

where R_T and R_s is the irradiance at the top of atmosphere and surface, respectively, P is the precipitation rate, L is the latent heat of vaporization, C is the difference of condensation and evaporation rates that does not lead to precipitation (i.e., cloud particles), and F_{sh} is the sensible heat flux at the surface. Note that multiplying diabatic terms by the density in Eq. (A11) converts the heating rate per unit mass to unit volume. Ice phase (e.g., snow precipitation) is ignored in using L. Also in Eq. (A11), we generally ignore LC, which is the rate of latent heat release by cloud particles that do not lead to precipitation and evaporation in the column. If 10% of cloud particles with the radius of 10 μm and concentration of 200 cm^{-1} filled in a 10-km column are exported from the column over a month (i.e., not evaporated in the column), the error neglecting LC in estimating the latent heat release in the column is less than 1 $\mathrm{W\,m}^{-2}$. Then Eq. (A10) is

$$\frac{1}{g}\frac{\partial}{\partial t}\int_0^{p_s}(c_pT+\Phi_s+k)\,dp+\frac{1}{g}\nabla_p\cdot\int_0^{p_s}\mathbf{U}(c_pT+\Phi+k)\,dp = (R_{\mathrm{TOA}}-R_s)+L(P+C)-F_{\mathrm{sh}}. \tag{A12}$$

Using a water mass balance equation,

$$\frac{1}{g}\frac{\partial}{\partial t}\int_0^{p_s}Lq\,dp=-\frac{1}{g}\nabla_p\cdot\int_0^{p_s}\mathbf{U}Lq\,dp-F_{\mathrm{lh}}-L(P+C) \tag{A13}$$

adding Eqs. (A12) and (A13) leads to,

$$\frac{1}{g}\frac{\partial}{\partial t}\int_0^{p_s}(c_pT+\Phi_s+k+Lq)\,dp+\frac{1}{g}\nabla_p\cdot\int_0^{p_s}\mathbf{U}(c_pT+\Phi+k+Lq)\,dp = (R_{\mathrm{TOA}}-R_{\mathrm{sfc}})-F_{\mathrm{sh}}-F_{\mathrm{lh}}, \tag{A14}$$

which is equivalent to Eq. (16) in Trenberth (1997). Equation (A14) can also be derived by equating the change of atmospheric energy integrated over the column with energy fluxes through top, bottom, and side boundaries.

REFERENCES

Adler, R. F., G. Gu, and G. J. Huffman, 2012: Estimating climatological bias errors for the Global Precipitation Climatology Project (GPCP). *J. Appl. Meteor. Climatol.*, **51**, 84–99, doi:10.1175/JAMC-D-11-052.1.

Behrangi, A., G. Stephens, R. F. Adler, G. J. Huffman, B. Lambrigsten, and M. Lebsock, 2014: An update on the oceanic precipitation rate and its zonal distribution in light of advanced observations from space. *J. Climate*, **27**, 3957–3965, doi:10.1175/JCLI-D-13-00679.1.

Berg, W., T. L'Ecuyer, and J. M. Haynes, 2010: The distribution of rainfall over oceans from spaceborne radars. *J. Appl. Meteor. Climatol.*, **49**, 535–543, doi:10.1175/2009JAMC2330.1.

Boer, G. J., 1982: Diagnostic equations in isobaric coordinates. *Mon. Wea. Rev.*, **110**, 1801–1820, doi:10.1175/1520-0493(1982)110<1801:DEIIC>2.0.CO;2.

Brown, P. J., and C. D. Kummerow, 2014: An assessment of atmospheric water budget components over tropical oceans. *J. Climate*, **27**, 2054–2071, doi:10.1175/JCLI-D-13-00385.1.

Chen, B., and C. Liu, 2016: Warm organized rain system over the tropical Pacific. *J. Climate*, **29**, 3403–3422, doi:10.1175/JCLI-D-15-0177.1.

Fasullo, J. T., and K. E. Trenberth, 2008: The annual cycle of the energy budget. Part I: Global mean and land–ocean exchanges. *J. Climate*, **21**, 2297–2312, doi:10.1175/2007JCLI1935.1.

Held, I. M., and B. J. Soden, 2006: Robust responses of the hydrological cycle to global warming. *J. Climate*, **19**, 5686–5699, doi:10.1175/JCLI3990.1.

Huffman, G. J., and Coauthors, 1997: The Global Precipitation Climatology Project (GPCP) combined precipitation dataset. *Bull. Amer. Meteor. Soc.*, **78**, 5–20, doi:10.1175/1520-0477(1997)078<0005:TGPCPG>2.0.CO;2.

Kato, S., 2009: Interannual variability of the global radiation budget. *J. Climate*, **22**, 4893–4907, doi:10.1175/2009JCLI2795.1.

——, and Coauthors, 2011: Improvements of top-of-atmosphere and surface irradiance computations with *CALIPSO*-, *CloudSat*-, and MODIS-derived cloud and aerosol properties. *J. Geophys. Res.*, **116**, D19209, doi:10.1029/2011JD016050.

——, N. G. Loeb, D. A. Rutan, F. G. Rose, S. Sun-Mack, W. F. Miller, and Y. Chen, 2012: Uncertainty estimate of surface irradiances computed with MODIS-, *CALIPSO*-, and *CloudSat*-derived cloud and aerosol properties. *Surv. Geophys.*, **33**, 395–412, doi:10.1007/s10712-012-9179-x.

——, ——, F. G. Rose, D. R. Doelling, D. A. Rutan, T. E. Caldwell, L. Yu, and R. A. Weller, 2013: Surface irradiances consistent with CERES-derived top-of-atmosphere shortwave and longwave irradiances. *J. Climate*, **26**, 2719–2740, doi:10.1175/JCLI-D-12-00436.1.

Lambert, F. H., and M. J. Webb, 2008: Dependency of global mean precipitation on surface temperature. *Geophys. Res. Lett.*, **35**, L16706, doi:10.1029/2008GL034838.

L'Ecuyer, T., and Coauthors, 2015: The observed state of the energy budget in the early twenty-first century. *J. Climate*, **28**, 8319–8346, doi:10.1175/JCLI-D-14-00556.1.

Loeb, N. G., B. A. Wielicki, D. R. Doelling, G. L. Smith, D. F. Keyes, S. Kato, N. Manalo-Smith, and T. Wong, 2009: Toward optimal closure of the earth's top-of-atmosphere radiation budget. *J. Climate*, **22**, 748–766, doi:10.1175/2008JCLI2637.1.

——, J. M. Lyman, G. C. Johnson, R. P. Allan, D. R. Doelling, T. Wong, B. J. Soden, and G. L. Stephens, 2012: Observed changes in top-of-the-atmosphere radiation and upper-ocean heating consistent within uncertainty. *Nat. Geosci.*, **5**, 110–113, doi:10.1038/ngeo1375.

——, D. A. Rutan, S. Kato, and W. Wang, 2014: Observing interannual variations in Hadley circulation atmospheric diabatic heating and circulation strength. *J. Climate*, **27**, 4139–4158, doi:10.1175/JCLI-D-13-00656.1.

——, H. Wang, A. Cheng, S. Kato, J. T. Fasullo, K.-M. Xu, and R. P. Allan, 2016: Observational constraints on atmospheric and oceanic cross-equatorial hear transports: Revising the precipitation asymmetry problem in climate models. *Climate Dyn.*, **46**, 3239–3257, doi:10.1007/s00382-015-2766-z.

Mayer, M., and L. Haimberger, 2012: Poleward atmospheric energy transport and their variability as evaluated from ECMWF reanalysis data. *J. Climate*, **25**, 734–752, doi:10.1175/JCLI-D-11-00202.1.

Neggers, R. A., J. D. Neelin, and B. Stevens, 2007: Impact mechanism of shallow cumulus convection on tropical climate dynamics. *J. Climate*, **20**, 2623–2642, doi:10.1175/JCLI4079.1.

Nuijens, L., B. Stevens, and A. P. Siebesma, 2009: The environment of precipitating shallow cumulus convection. *J. Atmos. Sci.*, **66**, 1962–1979, doi:10.1175/2008JAS2841.1.

Oreopoulos, L., N. Cho, D. Lee, S. Kato, and G. J. Huffman, 2014: An examination of the nature of global MODIS cloud regimes. *J. Geophys. Res. Atmos.*, **119**, 8362–8383, doi:10.1002/2013JD021409.

Peixoto, J. P., and A. H. Oort, 1992: *Physics of Climate*. American Institute of Physics, 520 pp.

Riehl, H., and J. Malkus, 1958: On the heat balance in the equatorial trough zone. *Geophysica*, **6**, 503–538.

Sassen, K., and Z. Wang, 2008: Classifying clouds around the globe with the *CloudSat* radar: 1-year of results. *Geophys. Res. Lett.*, **35**, L04805, doi:10.1029/2007GL032591.

Stephens, G. L., and C. D. Kummerow, 2007: The remote sensing of clouds and precipitation from space: A review. *J. Atmos. Sci.*, **64**, 3742–3765, doi:10.1175/2006JAS2375.1.

——, and T. D. Ellis, 2008: Controls of global mean precipitation increases in global warming GCM experiments. *J. Climate*, **21**, 6141–6155, doi:10.1175/2008JCLI2144.1.

——, and Coauthors, 2012: An update on Earth's energy balance in light of the latest global observations. *Nat. Geosci.*, **5**, 691–696, doi:10.1038/ngeo1580.

Trenberth, K. E., 1997: Using atmospheric budgets as constraint on surface fluxes. *J. Climate*, **10**, 2796–2809, doi:10.1175/1520-0442(1997)010<2796:UABAAC>2.0.CO;2.

——, and A. Solomon, 1993: Implications of global atmospheric spatial spectra for processing and displaying data. *J. Climate*, **6**, 531–545, doi:10.1175/1520-0442(1993)006<0531:IOGASS>2.0.CO;2.

——, and D. P. Stepaniak, 2003a: Covariability of components of poleward atmospheric energy transports on seasonal and interannual timescales. *J. Climate*, **16**, 3691–3705, doi:10.1175/1520-0442(2003)016<3691:COCOPA>2.0.CO;2.

——, and ——, 2003b: Seamless poleward atmospheric energy transports and implications for the Hadley circulation. *J. Climate*, **16**, 3706–3722, doi:10.1175/1520-0442(2003)016<3706:SPAETA>2.0.CO;2.

——, and ——, 2004: The flow of energy through the earth's climate system. *Quart. J. Roy. Meteor. Soc.*, **130**, 2677–2701, doi:10.1256/qj.04.83.

——, and L. Smith, 2009: The three dimensional structure of the atmospheric energy budget: Methodology and evaluation. *Climate Dyn.*, **32**, 1065–1079, doi:10.1007/s00382-008-0389-3.

——, and J. T. Fasullo, 2013: Regional energy and water cycles: Transport from ocean to land. *J. Climate*, **26**, 7837–7851, doi:10.1175/JCLI-D-13-00008.1.

——, L. Smith, T. Qian, A. Dai, and J. Fasullo, 2007: Estimates of the global water budget and its annual cycle using observational and model data. *J. Hydrometeor.*, **8**, 758–769, doi:10.1175/JHM600.1.

——, J. T. Fasullo, and J. Kiehl, 2009: Earth's global energy budget. *Bull. Amer. Meteor. Soc.*, **90**, 311–323, doi:10.1175/2008BAMS2634.1.

——, ——, and J. Mackaro, 2011: Atmospheric moisture transports from ocean to land and global energy flows in reanalyses. *J. Climate*, **24**, 4907–4924, doi:10.1175/2011JCLI4171.1.

Vallis, G. K., 2006: *Atmospheric and Oceanic Fluid Dynamics*. Cambridge University Press, 745 pp.

Vinukollu, R. K., E. F. Wood, C. R. Ferguson, and J. B. Fisher, 2011: Global estimates of evapotranspiration for climate studies using multi-sensor remote sensing data: Evaluation of three process-based approaches. *Remote Sens. Environ.*, **115**, 801–823, doi:10.1016/j.rse.2010.11.006.

Wielicki, B. A., and R. M. Welch, 1986: Cumulus cloud properties derived using Landsat satellite data. *J. Climate Appl. Meteor.*, **25**, 261–276, doi:10.1175/1520-0450(1986)025<0261:CCPDUL>2.0.CO;2.

Wild, M., and Coauthors, 2015: The energy balance over land and oceans: an assessment based on direct observations and CMIP5 climate models. *Climate Dyn.*, **44**, 3393–3429, doi:10.1007/s00382-014-2430-z.

Wilks, D. S., 1995: *Statistical Methods in the Atmospheric Sciences: An Introduction*. Academic Press, 467 pp.

Wolff, D. B., and B. L. Fisher, 2008: Comparisons of instantaneous TRMM ground validation and satellite rain-rate estimates at different spatial scales. *J. Appl. Meteor. Climatol.*, **47**, 2215–2237, doi:10.1175/2008JAMC1875.1.

Xu, K.-M., T. Wong, B. A. Wielicki, L. Parker, and Z. A. Eitzen, 2005: Statistical analyses of satellite cloud object data from CERES. Part I: Methodology and preliminary results of 1998 El Niño/2000 La Niña. *J. Climate*, **18**, 2497–2514, doi:10.1175/JCLI3418.1.

——, ——, S. Dong, F. Chen, S. Kato, and P. C. Taylor, 2016a: Cloud object analysis of CERES *Aqua* observations of tropical and subtropical cloud regimes, Part I: Four-year climatology. *J. Climate*, **29**, 1617–1638, doi:10.1175/JCLI-D-14-00836.1.

Zhang, Y.-C., W. B. Rossow, and P. W. Stackhouse Jr., 2006: Comparison of different global information sources used in surface radiative flux calculation: Radiative properties of the surface. *J. Geophys. Res.*, **112**, D01102, doi:10.1029/2005JD007008.